HHS Public Access

Author manuscript

*J Struct Biol*. Author manuscript; available in PMC 2025 March 17.

Published in final edited form as:

*J Struct Biol*. 2022 June ; 214(2): 107852. doi:10.1016/j.jsb.2022.107852.

# Exploring high-resolution cryo-ET and subtomogram averaging capabilities of contemporary DEDs

**Martin Obr**[a], **Wim J.H. Hagen**[b], **Robert A. Dick**[c], **Lingbo Yu**[d], **Abhay Kotecha**[d], **Florian K. M. Schur**[a,*]

[a]Institute of Science and Technology Austria (ISTA), Klosterneuburg, Austria

[b]European Molecular Biology Laboratory (EMBL), Heidelberg, Germany

[c]Department of Molecular Biology and Genetics, Cornell University, Ithaca, USA

[d]Materials and Structural Analysis Division, Thermo Fisher Scientific, Eindhoven, Netherlands

## Abstract

The potential of energy filtering and direct electron detection for cryo-electron microscopy (cryo-EM) has been well documented. Here, we assess the performance of recently introduced hardware for cryo-electron tomography (cryo-ET) and subtomogram averaging (STA), an increasingly popular structural determination method for complex 3D specimens. We acquired cryo-ET datasets of EIAV virus-like particles (VLPs) on two contemporary cryo-EM systems equipped with different energy filters and direct electron detectors (DED), specifically a Krios G4, equipped with a cold field emission gun (CFEG), Thermo Fisher Scientific Selectris X energy filter, and a Falcon 4 DED; and a Krios G3i, with a Schottky field emission gun (XFEG), a Gatan Bioquantum energy filter, and a K3 DED. We performed constrained cross-correlation-based STA on equally sized datasets acquired on the respective systems. The resulting EIAV CA hexamer reconstructions show that both systems perform comparably in the 4–6 Å resolution range based on Fourier-Shell correlation (FSC). In addition, by employing a recently introduced multiparticle refinement approach, we obtained a reconstruction of the EIAV CA hexamer at 2.9 Å. Our results demonstrate the potential of the new generation of energy filters and DEDs for STA, and the effects of using different processing pipelines on their STA outcomes.



*Corresponding author. florian.schur@ist.ac.at (F.K.M. Schur).

CRediT authorship contribution statement

**Martin Obr:** Conceptualization, Methodology, Software, Validation, Formal analysis, Investigation, Data curation, Writing – original draft, Writing – review & editing, Visualization. **Wim J.H. Hagen:** Conceptualization, Methodology, Investigation, Data curation, Writing – review & editing. **Robert A. Dick:** Methodology, Resources, Writing – review & editing. **Lingbo Yu:** Investigation. **Abhay Kotecha:** Conceptualization, Methodology, Investigation, Data curation, Writing – review & editing. **Florian K.M. Schur:** Conceptualization, Validation, Data curation, Writing – original draft, Writing – review & editing, Visualization, Supervision, Project administration, Funding acquisition.

Declaration of Competing Interest

The authors declare the following financial interests/personal relationships which may be considered as potential competing interests: Abhay Kotecha reports a relationship with Thermo Fisher Scientific Inc that includes: employment. Lingbo Yu reports a relationship with Thermo Fisher Scientific Inc that includes: employment.

Appendix A. Supplementary material

Supplementary data to this article can be found online at https://doi.org/10.1016/j.jsb.2022.107852.

**Keywords**

Cryo-electron microscopy; Cryo-electron tomography; Direct electron detectors; Subtomogram averaging

## 1. Introduction

Cryo-electron tomography (cryo-ET) is used to visualize complex biological environments in 3D. In combination with the image processing technique subtomogram averaging (STA), structures in their native context, such as the interior of cells, can be determined (Asano et al., 2016; Beck and Baumeister, 2016; Bykov et al., 2017; Guo et al., 2018; Turgay et al., 2017; Wang et al., 2022; Weiss et al., 2019; Zimmerli et al., 2021). In recent years, substantial developments in cryo-ET data acquisition and STA processing have resulted in high-resolution structures of challenging samples that are not accessible by any other method (Bäuerlein and Baumeister, 2021). However, while high-resolutions at sub-4 Å can now be reached for some specimens, such as ribosomes (O'Reilly et al., 2020; Tegunov et al., 2021), selected virus assemblies (Dick et al., 2020; Himes and Zhang, 2018; Mattei et al., 2018; Schur et al., 2016; Zivanov et al., 2022), bacterial surface proteins (Zivanov et al., 2022), and apoferritin or dNTPase *in vitro* (Bouvette et al., 2021; Ni et al., 2022; Tegunov et al., 2021), the proportion of entries in the Electron Microscopy Data Bank at <4 Å solved by STA in the period from 2016 to 2021 was only 1.7%. In the same period, for SPA the proportion of structures at this resolution was 54.4%.

Still, the potential of cryo-ET and its increasing popularity has led to a growing scientific community that is actively contributing to developments (for examples see (Chen et al., 2019; Himes and Zhang, 2018; Sanchez et al., 2020; Scaramuzza and Castaño-Díez, 2021; Tegunov et al., 2021)). Improving the attainable resolution and especially reducing the number of particles required to reach a given resolution via cryo-ET and STA is a matter of significant interest to the cryo-EM field.

Reasons for the overall lower resolution achieved in cryo-ET include the higher complexity specimen environments and larger, more variable macromolecular complexes, resulting in higher demands on data acquisition, and image processing. Tilt series acquisition and cryo-ET data processing with the goal of obtaining high resolutions is challenging due to several limitations inherent to the method (as reviewed in (Förster and Hegerl, 2007; Schur, 2019; Wan and Briggs, 2016)), some of these limitations are: 1) the requirement to distribute the available cumulative dose over a finite number of tilt angles, necessitating a very low exposure per image, resulting in a low signal-to-noise ratio (SNR) for each tilt (Dierksen et al., 1993; Hegerl and Hoppe, 1976; McEwen et al., 1995); 2) increased thickness of the sample, particularly at high tilts; 3) the accumulated beam-induced damage during tilt series acquisition (Glaeser, 1971); 4) an incomplete sampling of the tilt range, due to mechanical limitations of the stage (Turoňová et al., 2016); and 5) lower throughput due to longer acquisition time. The first three limitations cause an increased loss of high spatial frequency information in later tilts.

Of the above-mentioned limitations, the last point has recently been addressed in several developments that exploit efficient data acquisition methods, more stable stages, and faster cameras (Bouvette et al., 2021; Chreifi et al., 2019; Eisenstein et al., 2019). This has allowed obtaining datasets of hundreds of tomograms within a short time. However, points 1–4 constitute inherent limitations of cryo-ET, which have been shown to be most efficiently mitigated by better means of data acquisition. This includes using direct electron detectors (DEDs) with improved camera detective quantum efficiency (DQE) and energy-filters that remove inelastically scattered electrons, which leads to enhanced SNR. In addition, optimized acquisition schemes have been shown to mitigate these limitations to a certain degree (Bouvette et al., 2021; Hagen et al., 2017; Turoňová et al., 2020).

SPA cryo-EM has also benefited from a series of developments, such as improved electron sources, improved specimen holders, and better direct detection with higher camera frame rates. Recently, the new generation of DEDs and energy filters of two microscope hardware manufacturers (Thermo Fisher Scientific (TFS) with their combination of the Selectris X energy filter and Falcon 4 DED; and Gatan with their combination of the Bioquantum energy filter and K3 DED) led to exciting results in SPA, reaching to atomic resolution for apoferritin samples (Nakane et al., 2020; Zhang et al., 2020). Another recent study also achieved similar breakthrough atomic resolution on the same sample using an aberration-corrected aplanatic Titan Krios and a Falcon 3 DED (Yip et al., 2020). These studies demonstrated the potential of SPA cryo-EM for structural biology of well-ordered and homogenous protein samples.

To assess the potential of current cryo-EM systems for high-resolution cryo-ET and STA, we tested two systems, each equipped with the newest generation of DEDs and energy filters. We acquired cryo-ET data, first on a Krios G4, equipped with a cold field emission gun (CFEG), Selectris X energy filter, and Falcon 4 DED (referred to as **System 1** herein, installed at the TFS RnD facility, Eindhoven, NL). We then acquired data on a Krios G3i, equipped with a high-brightness Schottky field emission gun (XFEG), Gatan Bioquantum energy filter, and K3 DED (**System 2**, installed at EMBL Heidelberg, Germany).

The sample was Equine infectious anemia virus (EIAV) virus-like particles (VLPs), formed from a truncated variant of the main retrovirus structural protein Gag. The polyprotein Gag (consisting of the canonical domains matrix (MA), capsid (CA), and nucleocapsid (NC)) and its truncations (consisting of only individual domains or parts thereof) can be expressed recombinantly, purified, and then assembled *in vitro* to form VLPs reflecting architecture and organization of authentic virus particles (Bush and Vogt, 2014).

Retroviral VLPs are a well-suited sample to explore the limitations and the potential of cryo-ET and STA (Obr and Schur, 2019). In almost all cases, Gag-derived VLPs vary in size and curvature, and lack global symmetry, making each particle a unique object. This makes them almost intractable for SPA cryo-EM approaches, and a relevant sample for demonstrating the high-resolution cryo-ET potential of the employed hardware and software. In particular, although lacking global symmetry, the locally symmetric lattice arrangement of the CA domain within Gag, with C2, C3, and C6 symmetry axes, facilitates STA processing. These local symmetries effectively reduce the angular search space (and hence computation time)

and increase the available dataset size. In addition, using an *in vitro* assembly system permits preparation of VLPs in a defined concentration, allowing easier optimization of grid preparation.

For these reasons, retroviral VLPs were the first to reach resolutions better than 4 Å using cryo-ET and STA (Schur et al., 2016). They also have been frequently used for benchmarking of data acquisition (Turoňová et al., 2020), and have served as evaluation data for the development of various image processing software suites, such as novaCTF (Turoňová et al., 2017), Dynamo (Scaramuzza and Castaño-Díez, 2021), emClarity (Himes and Zhang, 2018), and M (Tegunov et al., 2021).

For our work, we used an EIAV Gag truncation construct with the capsid (CA), spacer peptide (SP), and nucleocapsid (NC) domains (referred to as CASPNC), which forms spherical and tubular VLPs *in vitro*. EIAV CASPNC VLPs were recently analyzed on a cryo-ET system equipped with the Gatan K2 DED, yielding a resolution of 3.7 Å (Dick et al., 2020). By using this sample, we were able to compare the results from the previous generation of DEDs with the results from the new DEDs.

For our evaluation, we employed two established pipelines for processing cryo-ET data (Fig. S1). First, we evaluated the performance of both systems with equally sized datasets. For this, we used an approach as employed in previous papers studying structures of retroviral Gag assemblies. This approach is based on tomogram reconstruction with 3D CTF correction using novaCTF and the AV3-derived subtomogram averaging/alignment pipeline (Dick et al., 2020; Förster et al., 2005; Obr et al., 2021; Turoňová et al., 2020, 2017).

In addition, we used an approach which included consecutive 3D refinement in Relion (Bharat et al., 2015) and multiparticle refinement steps in the software M. This workflow previously resulted in the highest resolution STA structure to date (Tegunov et al., 2021).

Here we report that data obtained on System 1 and System 2 yield sub-4 Å reconstructions from relatively small datasets, and with consistent quality of their respective maps. Processing the full dataset obtained from System 1 via iterative refinement in Relion and multi-particle refinement in M resulted in a 2.9 Å reconstruction. Our analysis demonstrates that each system, as well as their unique data acquisition settings are compatible with high-resolution STA.

In order to support community-based software developments, the datasets acquired on System 1 and 2, presented herein, are deposited to the EMPIAR database under the accession codes EMPIAR-10889 and EMPIAR-10963, respectively.

## 2. Results & discussion

### 2.1. Data acquisition and evaluation

EIAV CASPNC VLPs were vitrified and screened on a Glacios TEM at IST Austria (see methods for details). Grids with appropriate VLP distribution and ice quality were then shipped to System 1 at TFS Eindhoven. Tilt series were acquired on a single grid in the electron event representation (EER) format using the TFS Tomography software. At the

time of dataset processing, none of our STA software was compatible with native EER processing, so we summed the electron events into computational frames for subsequent processing.

We then sent the same grid to EMBL Heidelberg, where a second dataset was acquired on System 2 using SerialEM. By using the same VLP preparation on the same grid for acquisition on both systems, we aimed to diminish sample-related bias. At the same time, this also negatively affected the size of dataset 2, as the remaining number of appropriate available acquisition positions was limited.

Beyond being different in microscope and camera hardware the data acquisition on both systems differed in the selected slit width of the filter (10 eV for System 1, 20 eV for System 2). Because of the detector size differences, no settings on System1 and System 2 with equal pixel size or image area were available. Instead, we evaluated several options to achieve a meaningful comparison, all with specific advantages and disadvantages to the individual systems. Specifically, three pixel sizes for System 2 could have been chosen (1.38, 1.053 and 0.822 Å/px) to approximate the pixel size (1.176 Å/px) and image area of System 1. Choosing a larger pixel size than System 1 would have resulted in an almost twice as large field of view for System 2, not providing a meaningful comparison. The nearest smaller pixel size (1.053 Å) would still have led to a larger image area on System 2, while also offering improved DQE. Hence, the setting we chose (0.822 Å/px) meant acquiring with a smaller pixel size on System 2 (by 43%), with improved DQE, but also resulted in a reduced total image area for System 2 (by 40%; see Supplementary Table 1 for details on the acquisition settings). In order to further normalize the datasets during downstream processing, to use similar processing parameters such as box size, masks and bandpass filters, we Fourier cropped the data to the same pixel size.

Tilt series in both datasets contained large amounts of spherical and tubular VLPs (Fig. 1a-b), as previously reported for EIAV CASPNC assemblies (Dick et al., 2020). As expected, the hexameric arrangement of the CA domains, forming a lattice on the surface of tubes and spheres, was clearly resolved. For further evaluation of data quality, we performed defocus estimation using CTFFIND4 (Rohou and Grigorieff, 2015) (Fig. 1c,d). Both datasets showed accurate fitting of the contrast transfer function (CTF) up to +/− 40°tilt, judged by the achieved resolution of CTF-fitting (Fig. 1f,h) and the CTF fit rate (ratio between successful and all CTF fits for a given tilt angle) (Fig. 1e,g). In the tilt range between −30° and +24°; and −36° and +42°, no failed CTF fits were observed in the case of System 1 and System 2, respectively (Fig. 1e,g). Beyond ±40° tilt angles (the last third of the tilt series with the highest accumulated exposure dose) the successful fit rate was 67% and 86% for System 1 and System 2, respectively. Overall, data acquired on System 2 showed a slightly higher resolution of CTF fits. As there are several notable differences between the two datasets that could affect this result, it is difficult to assign a reason for the slightly improved fitting results. One explanation for this could be the smaller pixel size used for the acquisition on System 2, which could have been beneficial for CTF fitting.

Notably, CTF-fitting showed slightly higher reliability for defoci further from focus than 2 μm for both systems. All of the above observations suggest that both systems perform favorably at the low-dose conditions required for cryo-ET.

### 2.2. STA benchmark using novaCTF

Next, to further assess the performance of the respective systems and the quality of the corresponding datasets, we performed STA on spherical VLPs. We used the subtomogram averaging workflow, as published previously (Dick et al., 2020; Turoňová et al., 2020) with minor adaptations, which utilizes 3D-CTF corrected tomograms and a constrained cross-correlation-based subtomogram averaging/alignment routine of AV3 (Förster et al., 2005).

To allow an unbiased analysis we designed a processing strategy that is not influenced by varying VLP quality. Specifically, individual spherical VLPs can differ in the completeness of their CA protein lattice (i.e. due to VLPs being broken or incompletely assembled). This results in different extents of lattice edges, which are formed by incomplete hexamers (Tan et al., 2021). This can, if present in different abundance, have a negative effect on the resolution of the final maps. In addition, the alignment of the central hexamer depends also on its hexamer neighbors, which are contained within the alignment mask. Hence, after the initial subtomogram alignment, we selected only STA positions that were fully embedded in the lattice (meaning that they had six neighbors), in order to remove CA hexamers at the lattice edges from the analysis.

As the datasets from both systems substantially differed in size, we designed a strategy for using equally sized data subsets from each system. For System 1, we divided the full dataset (65,876 subvolumes after cleaning lattice edges) into three equal parts based on time of acquisition, and from each of these parts selected 20,000 subvolumes for alignments and generation of the final respective averages. The dataset acquired on System 2 contained 26,518 subvolumes, from which 20,000 were selected (for details see Materials and Methods and Supplementary Table 2). This approach yielded three and one equally-sized data subsets for System 1 and System 2, respectively.

We then took advantage of the inherent local symmetries of the processed spherical EIAV CASPNC VLPs. We aligned the respective datasets using C6 symmetry. We then generated final averages for all subsets applying C1 symmetry (20,000 asymmetric units, a.u.), C2 symmetry (40,000 a.u.), C3 symmetry (60,000 a.u.), and C6 symmetry (120,000 a.u.), without any additional alignments. We estimated the resolutions for all generated structures using the 0.143 and 0.5 Fourier shell correlation (FSC) criterion and used the resulting values to make B-factor plots for both criteria (Fig. 2). The B-factor plots showed mostly insignificant differences in resolution between the C1, C2, C3, and C6 symmetric averages of all data subsets from both systems (Fig. 2 a and b). In seven out of eight measurements the mean resolution estimate for reconstructions obtained from System 1 was higher by 0.1–0.2 Å than that of System 2. For one measurement of the C2-symmetrized averages, the 0.5 FSC criterion showed a difference of 0.6 Å. However, upon inspection of the corresponding FSC curve from System 2 (Fig. S2b, purple curve), we observed this larger difference to be

caused by a local dip in FSC near the 0.5 criterion, rather than the FSC curve for this dataset being dramatically different from the others.

For the C6-symmetric averages the final resolution at the 0.143 FSC criterion was between 3.8 and 3.9 Å (Fig. 2d, Fig. S2). The three selected subsets of System 1 yielded resolutions of 3.8, 3.9, and 3.8 Å, while the dataset of System 2 resulted in a reconstruction at 3.9 Å. Importantly, upon inspection of the FSC curves for all data subsets, one of the System 1 subsets showed improved resolution compared to the other two subsets (Fig. S2). As additional measurement we performed model vs map FSCs (Fig. S2e), employing pdb 6T64 as model, which was refined into a cryo-ET map of EIAV CASP solved at 3.7 Å (EMD-10384). This gave results consistent with the half-map FSCs. Hence, while the mean resolution obtained for System 1 was higher, the difference was less dramatic for two out of the three subsets from System 1.

Overall, the STA maps obtained for both systems were highly comparable in terms of quality. Differences in resolution of 0.1–0.2 Å can be considered rather negligible, especially in the context of a previous study, which benchmarked the influence of different tilt schemes on final map resolution (Turoňová et al., 2020). There, FSC results differed significantly more - by 0.3–2.8 Å - despite all data being acquired on the very same system. Hence, our results show that both of our systems perform comparably well at STA in the sub-4 Å resolution regime for small datasets, and that other experimental factors may dictate the achieved resolution. It is also important to point out that our results should not be interpreted as evidence that one system performs better than the other. Examples of experimental differences between the two datasets that may have affected the observed STA performance are described here. System 1 uses a cold FEG as electron source (E-CFEG), which provides a more coherent beam than the high-brightness Schottky FEG (XFEG) of System 2. The impact of a more coherent illumination on cryo-ET data acquisition has so far not been systematically explored. In case of the dataset acquired on System 2 the specimen condition might have been affected by increased deposition of contamination on the grid, due to multiple loading/ unloading events and shipping. Furthermore, the pixel size used for acquisition on System 2 was smaller, resulting in an improved DQE.

Overall, our evaluation allows one to assess the performance and suitability of the two systems for determining high-resolution cryo-ET and STA structures from moderately-sized datasets.

Next, we performed STA for the whole dataset acquired on System 1, using the AV3 subtomogram averaging routine. In addition to the particles fully embedded in the lattice, we also included particles at the edges, as long as they had at least 4 neighbors. By doing so, we aimed to maximize dataset size to determine the highest achievable resolution for the System 1 dataset using the AV3-based approach. We did not perform this step for System 2, as the data selected from System 2 for the benchmark presented in Fig. 2 already contained 75% of all subtomograms, which would have meant repeating prior analysis with only a small increase in dataset size. For System 1, this approach yielded ~110,000 particles for further analysis. Cross-correlation cleaning after the last alignment, to optimize the resolution determined via FSC, reduced the number of particles included in the final

reconstruction to ~62,000 (~373,000 a.u). This resulted in a 3.4 Å resolution structure (Fig. S3a). This corresponds to an increase of ~0.5 Å by using 3.1 times more data, compared to the resolutions shown for System 1 in Fig. 2.

Since this structure was at the identical resolution as the previously solved highest-resolution structure of a retrovirus CA assembly using the AV3-based processing pipeline (EMPIAR-10164, processed in (Turoňová et al., 2017)), we reasoned that at this point this may represent the maximally achievable resolution given the data set size and the processing approach.

### 2.3. Multiparticle refinement of System 1 and System 2 full datasets

To determine if employing an alternative processing approach could improve the final map resolution, we used a recently described software pipeline of Warp, Relion, and Multiparticle refinement in M, which reported the highest resolution cryo-ET and STA structure of a retroviral CA assembly at 3.0 Å (EMPIAR-10164, processed in (Tegunov et al., 2021)). By doing so we aimed to assess the performance of System 1 in the sub-4 Å regime (and also System 2, although we predicted a lower resolution due to the significantly smaller overall dataset size).

M employs local tilt-series alignment and refinement of the CTF model, as well as utilization of multiple molecular species for this step. We therefore exploited the presence of tubular VLPs (consisting of C2-symmetric CA hexamers) within our tomograms (see also Fig. 1a,b), which were distributed over the field of view in most tomograms and therefore represented valuable alignment features. Additionally, since the cross-correlation cleaning approach was not applicable when using Relion, we attempted to increase the homogeneity of the subvolumes used for refinement by a more stringent exclusion of subvolumes that deviate from ideal lattice geometry. In order to retain only subvolumes containing the structurally most similar local CA hexamers we employed a cleaning strategy based on local geometry, similar to what has been previously used for mature HIV-1 and RSV CA assemblies (Mattei et al., 2016; Obr et al., 2021) (see also Fig. S4 and Materials & Methods for more details).

For the dataset acquired on System 1, this processing pipeline resulted in a 2.9 Å resolution structure of the EIAV CA C6-symmetric hexamer from spherical VLPs (using ~466,000 a.u.) (Fig. 3) and a 3.2 Å resolution reconstruction of the EIAV CA C2-symmetric hexamer from tubular VLPs (using ~107,000 a.u.) (Fig. S3c), respectively. While the structures from AV3-based and Relion/M-based processing cannot be directly compared due to a different cleaning approach, the increase in resolution is nevertheless notable and cannot alone be explained by the further increased subvolume quality, contributing to the final average. Our results demonstrate the impact of iterative local tilt-series alignment and CTF model refinement.

The local resolution map of the C6-symmetric hexamer reveals that the most stable regions of the hexameric lattice are located at the trimerization interface (Fig. 3b,c). This is consistent with our previous work that identified the importance of this interface for immature EIAV lattice formation (Dick et al., 2020).

To verify the resolutions we obtained, and to test the effect of different masking strategies on FSC resolution estimates, we measured the resolution of our sub-3 Å map using two standard masks, as employed in other STA studies (Himes and Zhang, 2018; Schur et al., 2016; Tegunov et al., 2021; Turoňová et al., 2020, 2017). First, a cylindrical mask and second, a body-shaped mask (Fig. S5a), which better matches the shape of a single CA hexamer. For both masks, the FSC curves were nearly identical (Fig. S5b) and importantly, led to the same resolution estimates. This suggests that use of either masking approach, as long as the mask encompasses the whole central unit, and includes sufficient Gaussian smoothing, is acceptable for resolution estimates of continuous retroviral lattices.

We also subjected the dataset from System 2 to the same Relion/M processing pipeline. This dataset contained only 45% and 35% of the number of subvolumes from spherical and tubular VLPs respectively compared to data from System 1. The workflow employing multiparticle refinement resulted in a 3.3 Å structure of the EIAV CA C6 symmetric hexamer from spherical VLPs (~195,000 a.u.) (Fig. S3b) and a 3.6 Å structure of the EIAV CA C2 symmetric hexamer from tubular VLPs (from ~37,000 a.u.) (Fig. S3d).

Comparison of the C6-symmetric structures determined in this study, to the previously solved structure from an identical sample from data acquired on a Titan Krios G1 equipped with a Bioquantum K2 (Dick et al., 2020), revealed visible, but still very subtle differences (Fig. 4), despite the difference in resolution of up to 0.8 Å. An important consideration in this comparison is that the dataset acquired on the Gatan K2 system was not processed via multiparticle refinement, but instead using the pipeline shown in Fig. 2 and Fig. S3a.

## 3. Conclusions

Here we describe our assessment of the potential of two different EFTEM setups combining narrow-band energy filtering and the newest generation of DEDs for high-resolution structure determination using cryo-ET and STA.

Our results clearly show that both systems support high-resolution cryo-ET data collection and perform comparably in the ~4–6 Å resolution regime for our STA benchmark. Furthermore, our reconstruction at 2.9 Å demonstrates that System 1 is capable of collecting cryo-ET data that can be processed to sub-3 Å using STA. While the dataset for System 2 did not allow us to achieve the same resolution, likely due to particle number, the sub-3 Å subtomogram averaging capabilities of the K3 have recently been shown in a different publication (Tegunov et al., 2021).

However, the number of specimens which can currently reach sub-3 Å resolution via cryo-ET and STA is likely constrained to *in vitro (biochemically pure)* samples. Considering the increased use of cryo-ET for *in situ* structure determination, we believe that our observations at the resolutions between 4 and 6 Å, using smaller datasets, are of higher relevance. Based on the results presented here and in previous studies, appropriate cryo-ET data acquisition conditions, e.g. choice of the tilt scheme (Turoňová et al., 2020), might represent a more dominant factor for determining cryo-ET data quality, than the choice between systems equipped with latest generation DEDs.

Since pipelines supporting native EER processing were not available at the time of this publication, we have not explored all the options that the new data format makes available. Future studies should help determine if further advantages of the EER format are beneficial to STA.

## 4. Materials & methods

### 4.1. In vitro assembly of EIAV VLPs

EIAV CASPNC VLPs were assembled as previously described (Dick et al., 2020). Briefly, 30 μL assembly reactions containing 50 μM purified CASPNC protein, 500 mM NaCl, 10 μM IP6, 2 mM TCEP, and 10 μM GT50 oligonucleotide were dialyzed against buffer containing 20 mM MES pH 6.2, 100 mM NaCl, 2 mM TCEP, and 10 μM IP6 for 4 h at 4°C. To assess assembly, 5 μL of the assembly reaction was spotted on glow discharged (15 mA, 30 sec) grids (formvar/carbon 200), followed by 2% uranyl acetate staining, and imaging on a Morgagni transmission electron microscope.

### 4.2. Sample preparation for cryo-ET

Cryo-EM grids with CASPNC VLPs were prepared using a Leica GP2 plunger. 2.5 μL of EIAV CASPNC VLPs, mixed with 10 nm colloidal gold, were applied to glow discharged 2/2-C C-flat grids immediately before vitrification. The grids were then back-side blotted for 3.5 s at 10 °C and ~95% humidity, subsequently plunged into liquid ethane, and then transferred to liquid nitrogen for storage. The grids were screened on a 200 kV Glacios TEM using SerialEM software. Specifically, for each grid, a grid map and medium magnification maps on selected positions were acquired. The overall grid quality and distribution of particles were then taken as the criteria for grid selection. System 1 and System 2 data acquisition was performed on the same grid.

### 4.3. Krios G4 Selectris X Falcon 4 (System 1) data acquisition

The first dataset was acquired using a Krios G4 with cold field emission gun (CFEG; Thermo Fisher Scientific) and a Selectris X energy filter with a Falcon 4 detector (Thermo Fisher Scientific). Data were collected with TEM Tomography 5 software (Thermo Fisher Scientific). Tilt-series were recorded at a nominal magnification of × 105,000, corresponding to a pixel size of 1.179 Å. A dose-symmetric scheme was used to collect tilt-series from −60° to 60° at a step size of 3°. The CFEG was automatically flashed every ~8 h. Data were collected using the EER format of Falcon 4. The total dose per tilt was 3.5e/Å$^2$. A 10 eV slit was used. Eucentric height was performed once for the entire grid square using the stage tilt method in TEM Tomography 5 software. Regions of interest for data collection were determined manually. Tracking and focusing was applied before and after acquisition of each tilt step. The energy filter zero-loss peak was tuned once prior to data acquisition. The target defocus for each tilt series was changed over a range of −0.75 to −3.25 um in steps of 0.25 um.

### 4.4. Krios G3i Bioquantum K3 (System 2) data acquisition

The second dataset was acquired using a Krios G3i with a XFEG electron source (Thermo Fisher Scientific) and a BioQuantum energy filter with a K3 detector (Gatan). The grid

was mapped at the lowest possible magnification, suitable grid squares were identified and mapped at the lowest SA magnification, omitting the grid squares already collected on by System 1. Tilt series were acquired using the Tilt Controller in SerialEM (Mastronarde, 2005). The calibrated pixel size was 0.822 Ångstrom, and the exposure time 0.096 s, which allowed for 7 frames to be saved in LZW compressed uncorrected TIF format. A dose-symmetric scheme was used to collect tilt-series from −60° to 60° at a step size of 3°. The total dose per tilt was 3.7 e/Å$^2$. A 20 eV slit was used. For each tilt series the SerialEM Eucentric Fine procedure was run to set stage height, followed by alignment of the point of interest. Tracking and focusing was applied for each tilt step, at the end of each tilt series the energy filter zero-loss peak was refined, and a new K3 hardware dark reference acquired. The target defocus for each tilt series was changed over a range of −0.75 to −3.25 um in steps of 0.25 um.

### 4.5. NovaCTF/AV3 processing

The image processing workflow is schematically depicted in Fig. S1. The initial processing for both System 1 and System 2 datasets was done identically, with the exception that the raw EER files obtained via System 1 were aligned and summed into mrc stacks using Relion 3.1. The tif frames generated by System 2 were aligned and summed using the alignframes plugin in IMOD.

Prior to further processing, bad tilts (e.g. images that shifted significantly during acquisition or due to a blocked beam at high tilts) were removed. The stacks were then low-pass filtered according to the respective exposure dose in individual tilts (Grant and Grigorieff, 2015). IMOD (Kremer et al., 1996) was used for tilt series alignment and to generate 8x binned tomograms, filtered using the SIRT-like filter in IMOD for manual picking. Defocus was estimated using CTFFIND4 (Rohou and Grigorieff, 2015). The full tomograms were reconstructed in NovaCTF (Turoňová et al., 2017) with simultaneous 3D CTF correction using the multiplication algorithm. The slab thickness was set to 15 nm.

The initial positions for subtomogram averaging were obtained as previously described (Dick et al., 2020). Briefly, the centers of VLPs were marked and saved as models in 3dmod. Subtomograms were then extracted at positions on the surface of a sphere with a radius corresponding to the dimension of the respective VLP, using a custom MAT-LAB script.

Subtomogram averaging and alignment was performed in the AV3/TOM-based package SubTOM (https://github.com/DustinMorado/subTOM), as described (Dick et al., 2020). Throughout processing we also employed Dynamo functionalities (Castano-Diez et al., 2012). Specifically, subtomogram alignment was done at bin8, bin4, bin2, and bin1, while gradually advancing the low-pass filter and decreasing the Euler angle scanning step and range. The initial reference was created de novo using a single VLP. The initial reference was then symmetrized (C6) and used to align subtomograms from all VLPs of a single high-defocus tomogram. The resulting reference was used as a starting template for the alignment of the whole dataset at bin8. Following alignments, subvolumes with overlapping positions, positions which diverged away from the VLP surface, as well as positions with low cross-correlation were removed.

As described in the results, for the analysis of the data subsets, only subtomograms, which were not located at the edges of the lattice, were selected. Specifically, we removed subtomograms that had fewer than 6 neighbors after alignment at bin8 (Fig. S4). A conservative lowpass filter of 30 Å or lower was used up to the last iteration of bin4 processing to avoid over-refinement. After bin4 alignment subtomograms with grey scale values differing by more than 2 sigma from the mean of the entire dataset, were removed.

To generate equally sized datasets, the cleaned data obtained on System 1 was split into three equal parts based on time of acquisition, and 21,000 subtomograms were randomly selected from each dataset for further processing. For the dataset obtained on System 2, only one subset with 21,000 random subtomograms was generated due to the limiting amount of collected data. The four subsets were split into their respective odd and even half sets, which were then processed independently at bin2 with two rounds of alignments. After bin2 alignments 20,000 particles with the best cross-correlation values for each subset were retained. Finally, 3 rounds of alignment were performed at bin1.

To keep the processing parameters consistent between datasets from both systems, and since the expected resolution was far from the physical Nyquist frequency in the System 2 dataset (0.822 Å /pix corresponds to the Nyquist frequency of 1.644 Å), the subtomograms were cropped in Fourier space to approximately match the pixel size at which the Falcon 4 dataset was acquired (1.179 Å).

To obtain relevant subtomogram alignment parameters from the tubular VLPs for subsequent refinement in Relion and M, the processing in subTOM for tubes was done analogically to the processing for spheres, except using C2-symmetry and stopping after bin4 alignment, before proceeding with multiparticle refinement.

For processing the full System 2 dataset we included all subtomograms that had at least 4 neighbors after alignment at bin8. In addition, after the final alignment, the particles were cleaned using a cross-correlation threshold to maximize the resolution at the 0.143 FSC criterion.

### 4.6. Multiparticle refinement

For the System 1 dataset acquired on the Falcon 4 DED, EER files were summed using Relion 3.1 to yield 5 TIF frames for each tilt. Computed (Falcon 4) and raw (K3) frames were processed using Warp. The tilt series alignments from Etomo and subtomogram alignments from the NovaCTF/AV3 pipeline were imported into Warp version nb20201104 using the dynamo2m script package (https://github.com/alisterburt/dynamo2m)(Burt et al., 2021), and used for subtomogram reconstruction. Subtomograms were reconstructed at bin4 using Warp, and Autorefine 3D was performed in Relion 3.0.7e. These steps were repeated at bin2 to yield the starting positions for multi-particle refinement in M. For the multiparticle refinement we excluded particles, which were outliers in terms of local lattice geometry. Briefly, we excluded hexamers which had less than 3 neighbors fulfilling the geometry restraints specified in Fig. S4b,c. Subsequently, five rounds of multiparticle refinement were performed, gradually extending the refinement options (Supplementary Table 3, Supplementary Table 4). As previously described, to use similarly sized boxes and

masks for both systems, we processed the data from System 1 at its nominal pixel size (1.179 Å) and the data from System 2 at a pixel size of 1.1508 Å (corresponding to a Fourier cropping factor of 1.4). The refinement was performed analogously for both datasets, with the only exception being the different setup of tiles for image and volume warp, to account for the rectangular shape of the K3 camera.

### 4.7. Resolution estimation

The resolution of the final averages obtained via the NovaCTF/AV3 pipeline was determined by a phase-randomized mask-corrected FSC using a Gaussian filtered cylindrical mask (for example see Fig. S5a).

To verify the resolution of the map obtained using Multiparticle refinement, we assessed two different masks - a body mask generated using the pdb model of EIAV CA hexamer (pdb 6T64) (Fig. S5a) and the same tight cylindrical mask around one hexamer, which was used for the FSC of the AV3 pipeline results (Fig. S5a). The resolution was measured in MATLAB, as well as Relion. The results were consistent and supportive of the reported resolution regardless of which mask or software was used for the FSC calculation (Fig. S5b-c). The half maps of the M refinement were then combined, B-factor sharpened and filtered to the measured resolution in M using the cylindrical mask (Fig. S5a, left) (Rosenthal and Henderson, 2003). Visualization of tilt series, tomograms, and EM-densities was performed in MATLAB, IMOD (Kremer et al., 1996), UCSF Chimera (Pettersen et al., 2004), and Pymol (Schrodinger LLC, 2010).

## Supplementary Material

Refer to Web version on PubMed Central for supplementary material.

## Acknowledgements

This work was funded by the Austrian Science Fund (FWF) grant P31445 to F.K.M.S and the National Institute of Allergy and Infectious Diseases under awards R01AI147890 to R.A.D. This research was also supported by the Scientific Service Units (SSUs) of IST Austria through resources provided by Scientific Computing (SciComp), the Life Science Facility (LSF), and the Electron Microscopy Facility (EMF). We thank Dustin Morado for providing the software SubTOM for data processing. We also thank William Wan for critical reading of the manuscript and valuable feedback.

## Data availability

The electron microscopy density maps and representative tomograms have been deposited in the Electron Microscopy Data Bank (accession codes EMD-14031, EMD-14032, EMD-14033, EMD-14034, EMD-14035, EMD-14036, and EMD-14037). The EER and tif movies; and tilt series acquired on System 1 and System 2 have been deposited to the Electron Microscopy Public Image Archive (EMPIAR) under the accession codes: EMPIAR-10889 and EMPIAR-10963, respectively.

## References

Asano S, Engel BD, Baumeister W, 2016. In Situ Cryo-Electron Tomography: A Post-Reductionist Approach to Structural Biology. J. Mol. Biol 428 (2), 332–343. [PubMed: 26456135]

Bäuerlein FJB, Baumeister W, 2021. Towards Visual Proteomics at High Resolution. J. Mol. Biol 433 (20), 167187. 10.1016/j.jmb.2021.167187.

Beck M, Baumeister W, 2016. Cryo-Electron Tomography: Can it Reveal the Molecular Sociology of Cells in Atomic Detail? Trends Cell Biol. 26 (11), 825–837. [PubMed: 27671779]

Bharat TM, Russo C, Löwe J, Passmore L, Scheres SW, 2015. Advances in Single-Particle Electron Cryomicroscopy Structure Determination applied to Sub-tomogram Averaging. Structure 23 (9), 1743–1753. 10.1016/j.str.2015.06.026. [PubMed: 26256537]

Bouvette J, Liu H-F, Du X, Zhou Y.e., Sikkema AP, da Fonseca Rezende e Mello J, Klemm BP, Huang R, Schaaper RM, Borgnia MJ, Bartesaghi A, 2021. Beam image-shift accelerated data acquisition for near-atomic resolution single-particle cryo-electron tomography. Nat. Commun 12 (1) 10.1038/s41467-021-22251-8.

Burt A, Gaifas L, Dendooven T, Gutsche I, Jensen GJ, 2021. A flexible framework for multi-particle refinement in cryo-electron tomography. PLOS Biol. 19 (8), e3001319.

Bush DL, Vogt VM, 2014. In Vitro Assembly of Retroviruses. Annu. Rev. Virol 1 (1), 561–580. 10.1146/annurev-virology-031413-085427. [PubMed: 26958734]

Bykov YS, Schaffer M, Dodonova SO, Albert S, Plitzko JM, Baumeister W, Engel BD, Briggs JAG, 2017. The structure of the COPI coat determined within the cell. Elife 6. 10.7554/eLife.32493.

Castaño-Díez D, Kudryashev M, Arheit M, Stahlberg H, 2012. Dynamo: a flexible, user-friendly development tool for subtomogram averaging of cryo-EM data in high-performance computing environments. J. Struct. Biol 178 (2), 139–151. [PubMed: 22245546]

Chen M, Bell JM, Shi X, Sun SY, Wang Z, Ludtke SJ, 2019. A complete data processing workflow for cryo-ET and subtomogram averaging. Nat. Methods 16 (11), 1161–1168. 10.1038/s41592-019-0591-8. [PubMed: 31611690]

Chreifi G, Chen S, Metskas LA, Kaplan M, Jensen GJ, 2019. Rapid tilt-series acquisition for electron cryotomography. J. Struct. Biol 205 (2), 163–169. [PubMed: 30639925]

Dick RA, Xu C, Morado DR, Kravchuk V, Ricana CL, Lyddon TD, Broad AM, Feathers JR, Johnson MC, Vogt VM, Perilla JR, Briggs JAG, Schur FKM, Rey FA, 2020. Structures of immature EIAV Gag lattices reveal a conserved role for IP6 in lentivirus assembly. PLoS Pathog. 16 (1), e1008277. 10.1371/journal.ppat.1008277.

Dierksen K, Typke D, Hegerl R, Baumeister W, 1993. Towards automatic electron tomography II. Implementation of autofocus and low-dose procedures. Ultramicroscopy 49 (1–4), 109–120. 10.1016/0304-3991(93)90217-L.

Eisenstein F, Danev R, Pilhofer M, 2019. Improved applicability and robustness of fast cryo-electron tomography data acquisition. J. Struct. Biol 208 (2), 107–114. [PubMed: 31425790]

Förster F, Hegerl R, 2007. Structure Determination In Situ by Averaging of Tomograms. In: Methods in Cell Biology. Academic Press, pp. 741–767. 10.1016/S0091-679X(06)79029-X.

Förster F, Medalia O, Zauberman N, Baumeister W, Fass D, 2005. Retrovirus envelope protein complex structure in situ studied by cryo-electron tomography. Proc. Natl. Acad. Sci. USA 102 (13), 4729–4734. 10.1073/pnas.0409178102. [PubMed: 15774580]

Glaeser RM, 1971. Limitations to significant information in biological electron microscopy as a result of radiation damage. J. Ultrasructure Res. 36 (3–4), 466–482. 10.1016/S0022-5320(71)80118-1.

Grant T, Grigorieff N, 2015. Measuring the optimal exposure for single particle cryo-EM using a 2.6 Å reconstruction of rotavirus VP6. Elife 4. 10.7554/eLife.06980.

Guo Q, Lehmer C, Martínez-Sánchez A, Rudack T, Beck F, Hartmann H, Pérez-Berlanga M, Frottin F, Hipp MS, Hartl FU, Edbauer D, Baumeister W, Fernández-Busnadiego R, 2018. In Situ Structure of Neuronal C9orf72 Poly-GA Aggregates Reveals Proteasome Recruitment. Cell 172 (4), 696–705.e12. [PubMed: 29398115]

Hagen WJH, Wan W, Briggs JAG, 2017. Implementation of a cryo-electron tomography tilt-scheme optimized for high resolution subtomogram averaging. J. Struct. Biol 197 (2), 191–198. [PubMed: 27313000]

Hegerl R, Hoppe W, 1976. Influence of Electron Noise on Three-dimensional Image Reconstruction. Zeitschrift für Naturforsch. A 31 (12), 1717–1721. 10.1515/zna-1976-1241.

Himes BA, Zhang P, 2018. emClarity: software for high-resolution cryo-electron tomography and subtomogram averaging. Nat. Methods 15 (11), 955–961. 10.1038/s41592-018-0167-z. [PubMed: 30349041]

Kremer JR, Mastronarde DN, McIntosh JR, 1996. Computer Visualization of Three-Dimensional Image Data Using IMOD. J. Struct. Biol 116 (1), 71–76. 10.1006/jsbi.1996.0013. [PubMed: 8742726]

Mastronarde DN, 2005. Automated electron microscope tomography using robust prediction of specimen movements. J. Struct. Biol 152 (1), 36–51. [PubMed: 16182563]

Mattei S, Glass B, Hagen WJH, Kräusslich H-G, Briggs JAG, 2016. The structure and flexibility of conical HIV-1 capsids determined within intact virions. Science (80-.) 354 (6318), 1434–1437.

Mattei S, Tan A, Glass B, Müller B, Kräusslich H-G, Briggs JAG, 2018. High-resolution structures of HIV-1 Gag cleavage mutants determine structural switch for virus maturation. Proc. Natl. Acad. Sci 115, E9401–E9410. 10.1073/PNAS.1811237115. [PubMed: 30217893]

McEwen BF, Downing KH, Glaeser RM, 1995. The relevance of dose-fractionation in tomography of radiation-sensitive specimens. Ultramicroscopy 60 (3), 357–373. 10.1016/0304-3991(95)00082-8. [PubMed: 8525549]

Nakane T, Kotecha A, Sente A, McMullan G, Masiulis S, Brown PMGE, Grigoras IT, Malinauskaite L, Malinauskas T, Miehling J, Uchański T, Yu L, Karia D, Pechnikova EV, de Jong E, Keizer J, Bischoff M, McCormack J, Tiemeijer P, Hardwick SW, Chirgadze DY, Murshudov G, Aricescu AR, Scheres SHW, 2020. Single-particle cryo-EM at atomic resolution. Nature 587 (7832), 152–156. 10.1038/s41586-020-2829-0. [PubMed: 33087931]

Ni T, Frosio T, Mendonça L, Sheng Y, Clare D, Himes BA, Zhang P, 2022. High-resolution in situ structure determination by cryo-electron tomography and subtomogram averaging using emClarity. Nat. Protoc 17 (2), 421–444. 10.1038/s41596-021-00648-5. [PubMed: 35022621]

O'Reilly FJ, Xue L, Graziadei A, Sinn L, Lenz S, Tegunov D, Blötz C, Singh N, Hagen WJH, Cramer P, Stülke J, Mahamid J, Rappsilber J, 2020. In-cell architecture of an actively transcribing-translating expressome. Science (80-.) 369 (6503), 554–557.

Obr M, Ricana CL, Nikulin N, Feathers J-P-R, Klanschnig M, Thader A, Johnson MC, Vogt VM, Schur FKM, Dick RA, 2021. Structure of the mature Rous sarcoma virus lattice reveals a role for IP6 in the formation of the capsid hexamer. Nat. Commun 12, 3226. 10.1038/s41467-021-23506-0. [PubMed: 34050170]

Obr M, Schur FKM, 2019. Structural analysis of pleomorphic and asymmetric viruses using cryo-electron tomography and subtomogram averaging. Adv. Virus Res. 117–159. 10.1016/bs.aivir.2019.07.008. [PubMed: 31522703]

Pettersen EF, Goddard TD, Huang CC, Couch GS, Greenblatt DM, Meng EC, Ferrin TE, 2004. UCSF Chimera–a visualization system for exploratory research and analysis. J. Comput. Chem 25 (13), 1605–1612. 10.1002/jcc.20084. [PubMed: 15264254]

Rohou A, Grigorieff N, 2015. CTFFIND4: Fast and accurate defocus estimation from electron micrographs. J. Struct. Biol 192 (2), 216–221. [PubMed: 26278980]

Rosenthal PB, Henderson R, 2003. Optimal Determination of Particle Orientation, Absolute Hand, and Contrast Loss in Single-particle Electron Cryomicroscopy. J. Mol. Biol 333 (4), 721–745. 10.1016/j.jmb.2003.07.013. [PubMed: 14568533]

Sanchez RM, Zhang Y, Chen W, Dietrich L, Kudryashev M, 2020. Subnanometer-resolution structure determination in situ by hybrid subtomogram averaging - single particle cryo-EM. Nat. Commun 11, 3709. 10.1038/s41467-020-17466-0. [PubMed: 32709843]

Scaramuzza S, Castaño-Díez D, Jensen GJ, 2021. Step-by-step guide to efficient subtomogram averaging of virus-like particles with Dynamo. PLOS Biol. 19 (8), e3001318.

Schrodinger LLC, 2010. The PyMOL Molecular Graphics System, Version 1.3r1.

Schur FK, 2019. Toward high-resolution in situ structural biology with cryo-electron tomography and subtomogram averaging. Curr. Opin. Struct. Biol 58, 1–9. 10.1016/j.sbi.2019.03.018. [PubMed: 31005754]

Schur FKM, Obr M, Hagen WJH, Wan W, Jakobi AJ, Kirkpatrick JM, Sachse C, Kräusslich H-G, Briggs JAG, 2016. An atomic model of HIV-1 capsid-SP1 reveals structures regulating assembly and maturation. Science (80-.) 353 (6298), 506–508.

Tan A, Pak AJ, Morado DR, Voth GA, Briggs JAG, 2021. Immature HIV-1 assembles from Gag dimers leaving partial hexamers at lattice edges as potential substrates for proteolytic maturation. Proc. Natl. Acad. Sci 118, e2020054118 10.1073/pnas.2020054118.

Tegunov D, Xue L, Dienemann C, Cramer P, Mahamid J, 2021. Multi-particle cryo-EM refinement with M visualizes ribosome-antibiotic complex at 3.5 Å in cells. Nat. Methods 18 (2), 186–193. 10.1038/s41592-020-01054-7. [PubMed: 33542511]

Turgay Y, Eibauer M, Goldman AE, Shimi T, Khayat M, Ben-Harush K, Dubrovsky-Gaupp A, Sapra KT, Goldman RD, Medalia O, 2017. The molecular architecture of lamins in somatic cells. Nature 543 (7644), 261–264. 10.1038/nature21382. [PubMed: 28241138]

Turoňová B, Hagen WJH, Obr M, Mosalaganti S, Beugelink JW, Zimmerli CE, Kräusslich H-G, Beck M, 2020. Benchmarking tomographic acquisition schemes for high-resolution structural biology. Nat. Commun 11, 876. 10.1038/s41467-020-14535-2. [PubMed: 32054835]

Turoňová B, Marsalek L, Slusallek P, 2016. On geometric artifacts in cryo electron tomography. Ultramicroscopy 163, 48–61. 10.1016/j.ultramic.2016.01.002. [PubMed: 26916079]

Turoňová B, Schur FKM, Wan W, Briggs JAG, 2017. Efficient 3D-CTF correction for cryo-electron tomography using NovaCTF improves subtomogram averaging resolution to 3.4 Å. J. Struct. Biol 199 (3), 187–195. [PubMed: 28743638]

Wan W, Briggs JAG, 2016. Chapter Thirteen - Cryo-Electron Tomography and Subtomogram Averaging. In: Crowther RA (Ed.), Methods in Enzymology. Academic Press, pp. 329–367. 10.1016/bs.mie.2016.04.014.

Wang Z, Grange M, Pospich S, Wagner T, Kho AL, Gautel M, Raunser S, 2022. Structures from intact myofibrils reveal mechanism of thin filament regulation through nebulin. Science 375, eabn1934. 10.1126/science.abn1934.

Weiss GL, Kieninger A-K, Maldener I, Forchhammer K, Pilhofer M, 2019. Structure and Function of a Bacterial Gap Junction Analog. Cell 178 (2), 374–384. e15. 10.1016/j.cell.2019.05.055. [PubMed: 31299201]

Yip KM, Fischer N, Paknia E, Chari A, Stark H, 2020. Atomic-resolution protein structure determination by cryo-EM. Nature 587 (7832), 157–161. 10.1038/s41586-020-2833-4. [PubMed: 33087927]

Zhang K, Pintilie GD, Li S, Schmid MF, Chiu W, 2020. Resolving individual atoms of protein complex by cryo-electron microscopy. Cell Res. 30 (12), 1136–1139. 10.1038/s41422-020-00432-2. [PubMed: 33139928]

Zimmerli CE, Allegretti M, Rantos V, Goetz SK, Obarska-Kosinska A, Zagoriy I, Halavatyi A, Hummer G, Mahamid J, Kosinski J, Beck M, 2021. Nuclear pores dilate and constrict in cellulo. Science (80-.) 374, eabd9776. 10.1126/science.abd9776.

Zivanov J, Otón J, Ke Z, Qu K, Morado D, Castaño-Díez D, von Kügelgen A, Bharat TAM, Briggs JAG, Scheres SHW, 2022. A Bayesian approach to single-particle electron cryo-tomography in RELION-4.0. bioRxiv 2022.02.28.482229. 10.1101/2022.02.28.482229.

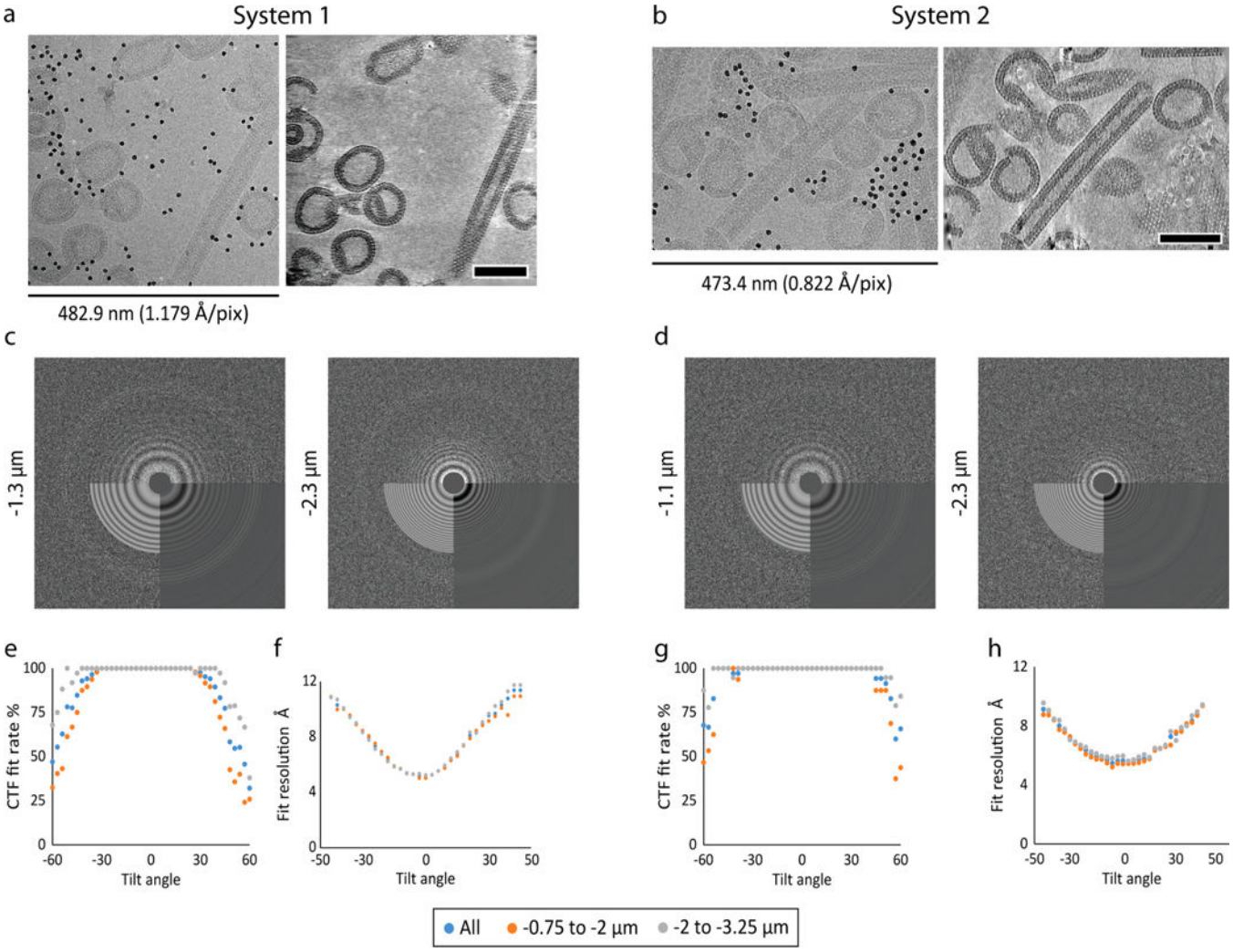


**Fig. 1.**

Cryo-electron tomography on current energy-filtered DEDs. a) Tilt image and reconstructed cryo-electron tomogram acquired on System 1 with a defocus of −2.8 µm. Left: 2D cryo-EM micrograph showing a single (0°) tilt. Right: 9.4 nm slice through the reconstructed tomogram. **b**) Tilt image and reconstructed cryo-electron tomogram acquired on System 2 with a defocus of −3 µm. Left: 2D cryo-EM micrograph showing a single (0°) tilt. Right: 9.9 nm slice through the reconstructed tomogram. The dimension of the x-axes is annotated for both systems. Scale bars are 100 nm. **c-d)** Representative CTFFIND4 outputs for the 0° tilt of two tilt series, acquired at different defocus settings, for System 1 (c) and System 2 (d). The upper part of the power spectrum shows the experimental power spectrum, the lower right panel shows the radial average and the lower left panel shows the estimated CTF-fit. The maximum fitted resolution in panels c and d (from left to right) is: 4.96 Å, 4.96 Å, 4.72 Å, 5.29 Å. **e-h)** Success rates for CTF fitting (e,g) and the median resolution of the CTF fitting (f,h) for each tilt, described by the highest spatial frequency to which the fit was reliable. (e-f) Show results for System 1, and (g-h) for System 2.

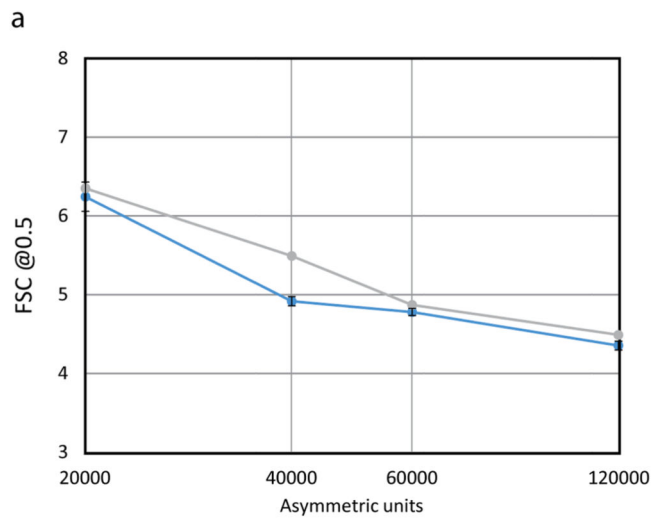


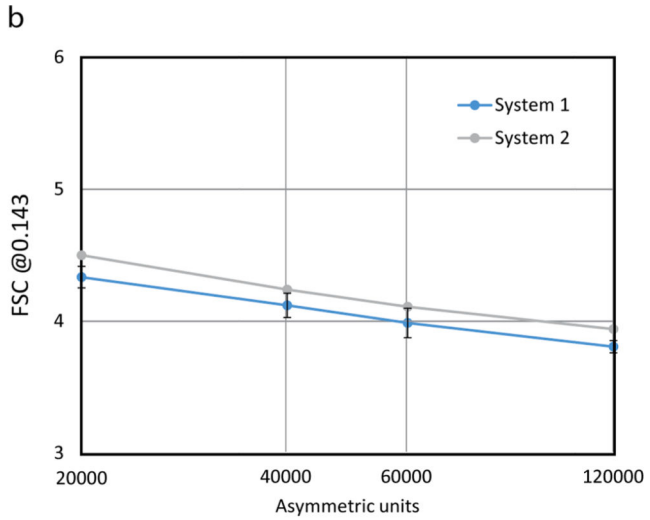


c

FSC @0.5

| | | C1 | C2 | C3 | C6 |
|---|---|---|---|---|---|
| System 1 | batch1 | 6.3 | 5.0 | 4.8 | 4.4 |
| | batch2 | 6.4 | 5.0 | 4.8 | 4.4 |
| | batch3 | 6.1 | 4.9 | 4.7 | 4.3 |
| | SD | 0.16 | 0.07 | 0.06 | 0.06 |
| | Mean | **6.2** | **4.9** | **4.8** | **4.4** |
| System 2 | | **6.4** | **5.5** | **4.9** | **4.5** |

d

FSC @0.143

| | | C1 | C2 | C3 | C6 |
|---|---|---|---|---|---|
| System 1 | batch1 | 4.4 | 4.2 | 4.0 | 3.8 |
| | batch2 | 4.4 | 4.1 | 4.1 | 3.9 |
| | batch3 | 4.3 | 4.0 | 3.9 | 3.8 |
| | SD | 0.07 | 0.09 | 0.11 | 0.05 |
| | Mean | **4.4** | **4.1** | **4.0** | **3.8** |
| System 2 | | **4.5** | **4.2** | **4.2** | **3.9** |

**Fig. 2.**

Subtomogram averaging resolution benchmark. Different symmetries (C1, C2, C3, C6) were applied to the maps for FSC measurements to assess the influence of dataset size and symmetry on resolution. **a)** FSC values at the 0.5 criterion plotted as a function of the number of asymmetric units. **b)** FSC values at 0.143 criterion plotted as a function of the number of asymmetric units. The curves for System 1 originate from the mean value of the measurements from the three subsets. X-axis in logarithmic scale in a,b. **c)** Resolution values in Å at the 0.5 FSC criterion, measured for different data-subsets from System 1 and System 2. **d)** Same as c, for values obtained at the 0.143 FSC criterion. SD is standard deviation.

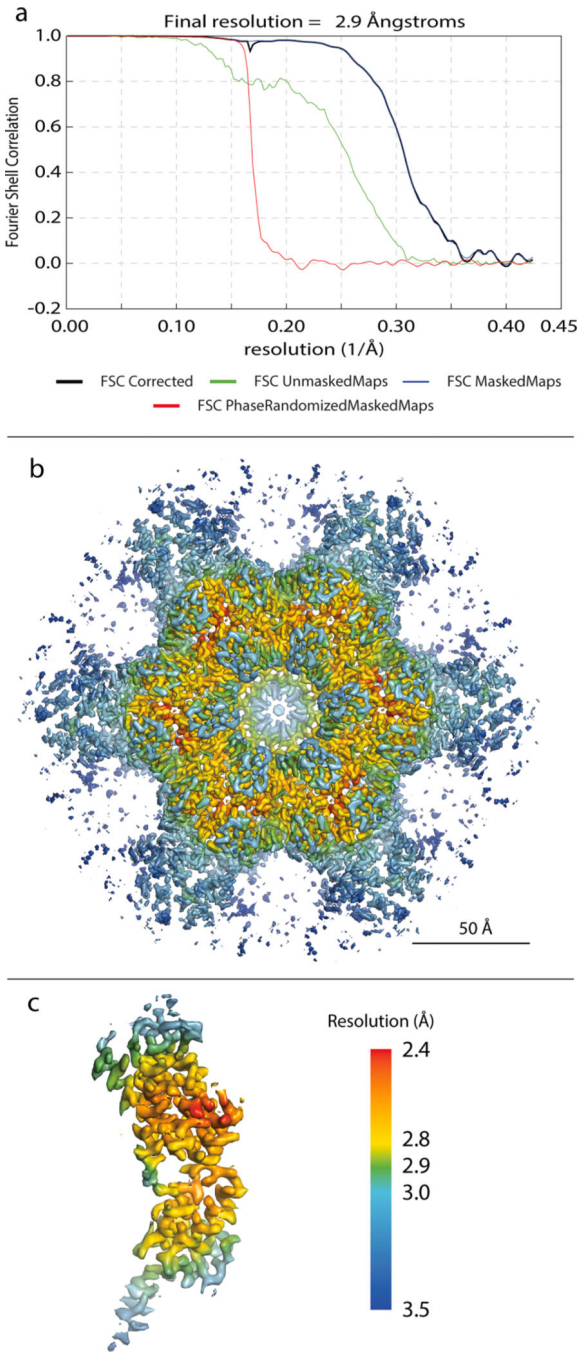


**Fig. 3.**

2.9 Å EIAV CA hexamer structure solved by multiparticle refinement using the full dataset acquired on System 1. a) FSC-curve. b-c) Structure of the full C6-symmetric hexamer (b) and one monomer (c) colored according to the local resolution as reported by M. The resolution range is depicted in the color bar.

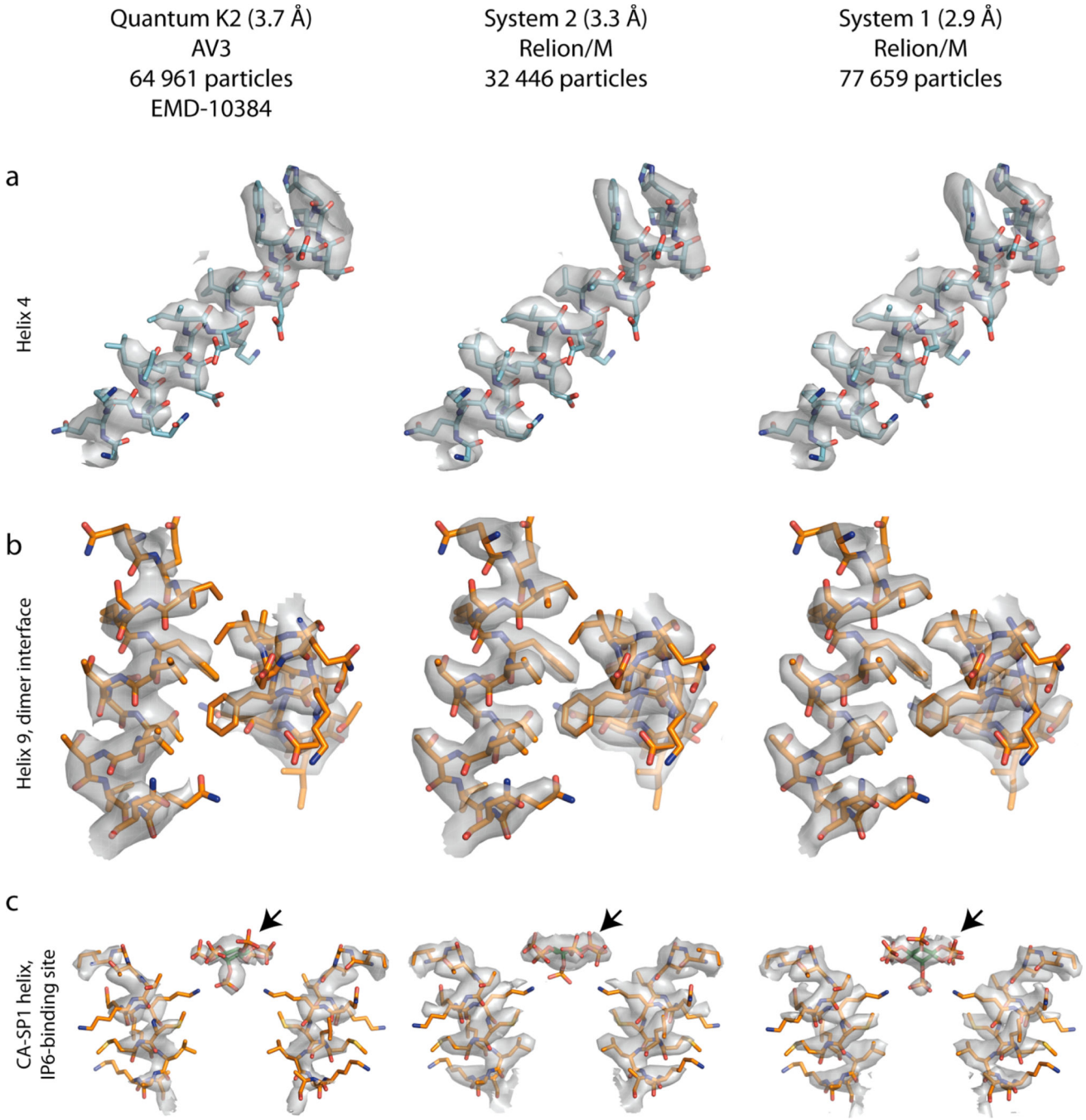


**Fig. 4.**

Gallery of EIAV-CASP structures solved using different detectors. Representative EM-densities from the structures generated via Relion/M in this study (center and right) and a structure determined previously using novaCTF/AV3 and the previous generation of the Gatan DED (left). The model for EIAV CA (pdb 6T64) fitted into the EM densities is consistent with all three structures. Notably, the density for IP6, a small molecule employed by EIAV for stabilizing the immature CA lattice, is best resolved within the lowest-resolution structure. **a)** Helix 4 in the N-terminal domain of EIAV CA; **b)** helix 9 in

the C-terminal domain of EIAV CA, forming an important dimeric inter-hexamer interface; **c)** Inositolhexakiphosphate (IP6) binding pocket, for clarity only two opposite helices from the 6-helix bundle are shown. IP6 is annotated by an arrow.